EES Solar

ROYAL SOCIETY OF CHEMISTRY

PAPER

View Article Online
View Journal | View Issue

Check for updates

Cite this: *EES Sol.*, 2025, **1**, 1051

'Ion-freeze' efficiency in perovskite solar cells: time scales for ion immobilization

Enrique H. Balaguera, *[a] F. Javier Marinelli Pra,[a] Chittaranjan Das,[b] Lorenzo Torresani,[b] Juan Bisquert [c] and Michael Saliba *[bd]

Received 25th August 2025
Accepted 28th August 2025

DOI: 10.1039/d5el00137d

rsc.li/EESSolar

It is essential to shed light on the complex multiscale dynamics of mobile ions in perovskite solar cells for developing efficiency testing protocols, gaining a deeper understanding of the degradation mechanisms, improving long-term stability, and, ultimately, driving the commercialization of this technology. This study provides characteristic times for inhibiting the presence of mobile ions in efficiency measurements, enabling a comparison between 'ion-freeze' and steady-state efficiencies to quantify ion-induced degradation losses. Using current transient analysis during current–voltage measurements for a wide range of sweep rates, we achieve precise time-scale mapping of the complex ionic landscape of perovskites, spanning from ion immobilization (at time scales much shorter than the diffusion rate) to the equilibrium situation, encompassing the ubiquitous hysteresis effects for which we define a scan-rate range of occurrence. We corroborate the theory by using Impedance Spectroscopy. Our study provides valuable information about the intricate ionic dynamics in the context of classical current–voltage measurements, supporting the integration of these complementary experiments into the foundational characterization practices of the perovskite photovoltaic community.

Broader context

Perovskite solar cells have reached exceptional levels of power conversion efficiency; however, concerns about their long-term stability continue to hinder their roadmap toward commercial viability. A central issue among the degradation pathways is the behavior of mobile ions, recognized as the major contributor to the loss of efficiency and operational instability in perovskite photovoltaics. A detailed analysis of the intricate multiscale dynamics of mobile ions is therefore pivotal for advancing standardized device characterization, elucidating degradation phenomena, enhancing operational stability, and propelling the broader adoption of this emerging photovoltaic technology. Characteristic times necessary to suppress ionic contributions during performance evaluations are investigated here through a systematic current transient analysis across a spectrum of voltage sweep rates. The temporal landscape governing ion dynamics of perovskites enables a quantitative distinction between steady-state and 'ion-freeze' efficiencies, offering a direct measure of degradation attributable to ionic motion. In this sense, a hysteresis domain is defined within a specific scan-rate interval. Theoretical insights are substantiated through Impedance Spectroscopy, reinforcing the interpretive framework. Collectively, our findings enrich the understanding of ionic behavior in perovskite materials and advocate for the integration of such methodologies into the toolkit for device characterization within the perovskite research community.

Introduction

Although perovskite solar cells hold significant potential to compete as strong contenders in the photovoltaic market due to the meteoritic growth in their power-conversion efficiency shown in recent years, the long-term stability of this technology is still behind that of commercially established silicon-based photovoltaics.[1,2] Specifically, metal halide perovskite solar cells are vulnerable to a range of stressors and can undergo multiple degradation mechanisms,[3] which can either be dominated by a single process or arise from the interplay of multiple competing factors.[4]

One of the most common underlying causes of these degradation pathways is the migration of mobile ions,[5] as an intrinsic property of the perovskite absorber material. However, this process can also have beneficial effects on freshly prepared or well-passivated photovoltaic devices.[6,7] Current–voltage characteristics are therefore compromised by transient ionic effects,[8,9] making their understanding crucial for minimizing changes in performance over time and, ultimately, the device optimization process.[10]

A new methodology to quantify mobile ion-induced efficiency losses to the device performance in perovskite

---

[a] *Escuela Superior de Ciencias Experimentales y Tecnología, Universidad Rey Juan Carlos, C/ Tulipán, s/n, 28933 Móstoles, Madrid, Spain. E-mail: enrique.hernandez@urjc.es*

[b] *Institute for Photovoltaics (ipv), University of Stuttgart, Pfaffenwaldring 47, 70569 Stuttgart, Germany. E-mail: michael.saliba@ipv.uni-stuttgart.de*

[c] *Instituto de Tecnología Química (Universitat Politècnica de València-Agencia Estatal Consejo Superior de Investigaciones Científicas), Av. dels Tarongers, 46022, València, Spain*

[d] *Helmholtz Young Investigator Group FRONTRUNNER, IMD-3 Photovoltaics, Forschungszentrum Jülich, Jülich, 52425, Germany*

photovoltaics was recently presented in the literature using fast hysteresis measurements.[11] This technique allows one to determine the steady-state and the 'ion-freeze' efficiencies, as real and virtual metrics of the device performance, respectively.[12]

On the one hand, the steady-state efficiency η_{ss}, obtained from stabilized current–voltage curves, refers to the condition at which mobile ions are effectively in equilibrium and fully responding to the applied voltage.[13] It is achieved when the voltage sweep rate is substantially slower than the diffusion rate (a few hundred of mV s^{-1}). The 'ion-freeze' efficiency $\eta_{\text{ion-freeze}}$, on the other hand, represents the cell performance measured under conditions where the movement of mobile ions is effectively suppressed.[11,12,14] To effectively immobilize the ionic charges, the hold time along the stepwise scanning should be sufficiently short to ensure that the mobile ions are "frozen" in time (ultra-fast scan rates in the sense of a few hundred V s^{-1}).

The difference between fast and slow scan speeds, related, respectively, to 'ion-freeze' and steady-state efficiencies (that is, $L_{\text{ion}} = \eta_{\text{ion-freeze}} - \eta_{ss}$), provides a value that quantifies the performance losses caused by mobile ions in perovskite solar cells.[12] Both limiting cases yield identical curves in the respective forward and reverse sweeps; however, hysteresis effects emerge in the current–voltage curves[15] at intermediate scan speeds. The magnitude and rate of the 'peak hysteresis' or the maximum difference between the efficiency determined from the forward *vs.* the reverse scan is indeed a critical tool for the diagnosis of the relationship between ion migration dynamics and device performance.[16–18]

The origin and interpretation of hysteresis and the steady-state efficiency have been thoroughly addressed in the literature, thanks to extensive collaborative research efforts. However, there are still no consolidated theoretical principles that explain the internal physical processes behind the 'ion-freeze' current–voltage curves within realistic time scales that reflect the complex ionic behavior of metal halide perovskites.

In this work, we endorse the concept of 'ion-freeze' efficiency, inspired by the works of Stolterfoht and coworkers,[5,11,12,14] as a novel approach to be used as a key parameter for emerging characterization protocols in assessing ion-induced device performance losses of high-performance perovskite solar cells.

From current–voltage measurements at different scan rates, we first corroborate the experimental results provided by literature. Using an advanced stepwise transient analysis, we demonstrate that only the fast or pure component of the recombination processes affects the evolution of the 'ion-freeze' current–voltage curves.

If any part of this recombination shifts to the slow ion-controlled regime of recombination, the value of $\eta_{\text{ion-freeze}}$ will change upon ageing. As the scan rate is reduced, the fast recombination mechanisms are complemented by ion-induced effects, including slow recombination processes, polarization mechanisms or even electric field screening, both in pristine conditions and after degradation.

We establish that the transition between consecutive current recordings in the voltage sweep is abruptly modified as a function of the speed rates and ageing time. From a physical model, we therefore explain the evolution of the experimental current–voltage curves, deciphering the time parameter that effectively leads to ion immobilization in a stepwise current–voltage scanning while further revealing the "game of dominance *vs.* loss of relevance" of physical effects in the current responses over time. A merit formula is derived to indicate the window of scan rates in which the experimentalists obtain current–voltage curves with hysteresis. Finally, impedance analysis was carried out for verification purposes.

Experimental

Fabrication of perovskite solar cells

Pre-patterned glass/indium tin oxide (ITO) substrates were cleaned by immersion in 2% volume Mucasol in water, acetone, isopropyl alcohol (IPA), while sonicating for 15 minutes each time. After each step, the substrates are rinsed with the next solvent. The substrates are then dried with a N_2 flow before they undergo a 30 minute ultraviolet (UV)/ozone treatment. The electron transport layer (ETL) of tin(IV) oxide (SnO_2) was deposited by spin coating (3000 rpm, 1000 rpm s^{-1}, 30 s) 100 µl of a 19 mg ml^{-1} solution in ethanol of $SnCl_2$, that is later converted to SnO_2 by heating to 200 °C for 1 hour in air.

The triple-cation perovskite precursor was prepared by wet chemistry methods. From powder-based precursors, 800 mg of PbI_2 into 1157 µl of a 4 : 1 mix of dimethylformammide (DMF) and dimethylsulfoxide (DMSO), and 150 mg of $PbBr_2$ were dissolved into 272 µl of the solvent mix. Subsequently, 220 mg of formamidinium iodide (FAI) were dissolved into 1029 µl of the PbI_2 solution, and 20 mg of methylammonium bromide (MABr) were dissolved into 143 µl of the $PbBr_2$ solution. Finally, we mix 930 µl of the $FAPbI_3$ solution, 70 µl of $MAPbBr_3$ and 52.6 µl of a 40 mg ml^{-1} solution of cesium iodide (CsI) in DMSO. The solution is kept at rest in the dark before deposition. The 2,2′,7,7′-tetrakis[*N*,*N*-di(4-methoxyphenyl)amino]-9,9′-spiro-bifluorene (Spiro-OMeTAD) solution was prepared by dissolving 92 mg of Spiro-OMeTAD powder into 1 ml of chlorobenzene, to which 21 µl of a 520 mg ml^{-1} solution of bis(trifluorometano) sulfonimida lithium salt (LiTFSI) into acetonitrile, 15 µl of a 150 mg ml^{-1} Co(III) TFSI salt (CoTFSI) in acetonitrile and 32 µl of tributyl phosphate (TBP) were added.

The perovskite precursor (80 µl) was spin-coated on the glass/ITO/SnO_2 substrate in two steps, a slow step (1000 rpm, 1000 rpm s^{-1}, 10 s) and a fast step (5000 rpm, 2000 rpm s^{-1}, 30 s). The solvent was removed by dropping an antisolvent (240 µl of chlorobenzene) 5 seconds before the end of the last step. The layer was finalized by annealing at 100 °C for 30 minutes. The layers are cooled down to room temperature and a solution of phenyl ethyl ammonium iodide (PEAI) 10 mg ml^{-1} in 2-propanol (IPA) is dynamically spin coated (4000 rpm, 1000 rpm s^{-1}, 30 s) on the perovskite layer. A subsequent annealing at 100 °C for 1 minute ensures the formation of the 2D perovskite.

Spiro-OMeTAD was spin casted (4000 rpm, 2000 rpm s^{-1}, 30 s) on the perovskite layer after it cooled down. The samples were left to oxidize overnight. The 100 nm golden contacts were thermally evaporated on the stack to finalize the device.

Characterization protocols

The current density–voltage curves for the perovskite solar cells were measured using a Keithley 2450 source meter under a standard Newport VeraSol-2 LED class AAA solar simulator. The lamp was calibrated using a NIST-certified KG3 filtered Si reference cell. The mask area was 0.16 cm^2 and the cells were measured at room temperature. We use scan rates from 1000 V s^{-1} to 0.1 V s^{-1} to determine the hysteresis behavior.

Beyond electrical measurements were carried out with a PGSTAT302N potentiostat/galvanostat, equipped with an impedance and ultra-fast sampling module, FRA32M and ADC10M, respectively, from Metrohm AutoLab. Impedance measurements were developed by configuring the AutoLab to apply sinusoidal signals of 10 mV amplitude from 1 MHz to 1 Hz at open-circuit voltage (V_{oc}). On the other hand, chronoamperometric experiments were carried out, immediately after frequency resolved measurements, by applying a constant signal with the value of V_{oc} and, after, voltage-excited steps of 5 mV. A sampling rate of 10 MHz and 10 kHz was used to record the initial-decay fast region and the subsequent slow relaxation of the current responses of perovskite solar cells, respectively.

All the experiments at room temperature were carried out under ambient atmosphere with the dry-air flow. The reproducibility of our conclusions was assured by conducting experiments in 10 samples with the same device configuration.

Results and discussion

Evolution of performance parameters as a function of the scan rate

To start with, we present representative performance data of a photovoltaic perovskite, reaching efficiencies up to 19%, with a *nip*-type configuration consisting of ITO/SnO$_2$/perovskite (Cs$_{0.05}$FA$_{0.88}$MA$_{0.07}$PbI$_{2.79}$Br$_{0.21}$)/PEAI/Spiro-OMeTAD/Au. We explore the impact of mobile ions on device degradation using the standardized dark storage protocol of ISOS-D-1 to obtain information on the cell's shelf life or the tolerance to ambient conditions.[19] Specifically, our samples were stored in the dark under ambient conditions, with a relative humidity ranging between 30 and 50%.

In the sequel, we use an 'ion-freeze' method that provides results of ion-induced losses by inhibiting the redistribution of mobile ions from their equilibrium positions at sufficiently high scan rates in comparison to equilibrium state. The evolution of the performance parameters of our perovskite solar cells with current–voltage sweep rate is shown in Fig. 1: (a) efficiency η, (b) short-circuit current density j_{sc}, (c) V_{oc}, and (d) fill factor (FF).

Firstly, we detect in Fig. 1a that the presence of mobile ions affects the device performance or 'ion-freeze' efficiency even when they are immobilized: comparing η at ultra-fast scan and slow scan rates, a slight decrease is observed, attributed to an inhomogeneous redistribution throughout the perovskite active layer that influences the fast step of recombination.[20] This reduction of $\eta_{\text{ion-freeze}}$ at fast scan rates (1000 V s^{-1}) is minimal compared to the pronounced change of η_{ss} observed during ageing in the slow range of 500 mV s^{-1} and 100 mV s^{-1}. As the samples degrade, the hysteresis effects also extend over a wider range of scan rates, evidencing a slower ionic response over time.[10,21,22] An additional indicator is the gradual shift of the 'peak hysteresis' towards slower scan rates, underscoring the strong dependence of hysteresis behavior on the degradation state of the device.[23]

It is important to point out that, for the fresh samples, the main reason for the ionic loss in efficiency is the decay of approximately 1 mA cm^{-2} in j_{sc} (calculable from the comparison in equilibrium and 'ion-freeze' states). On the other hand, the

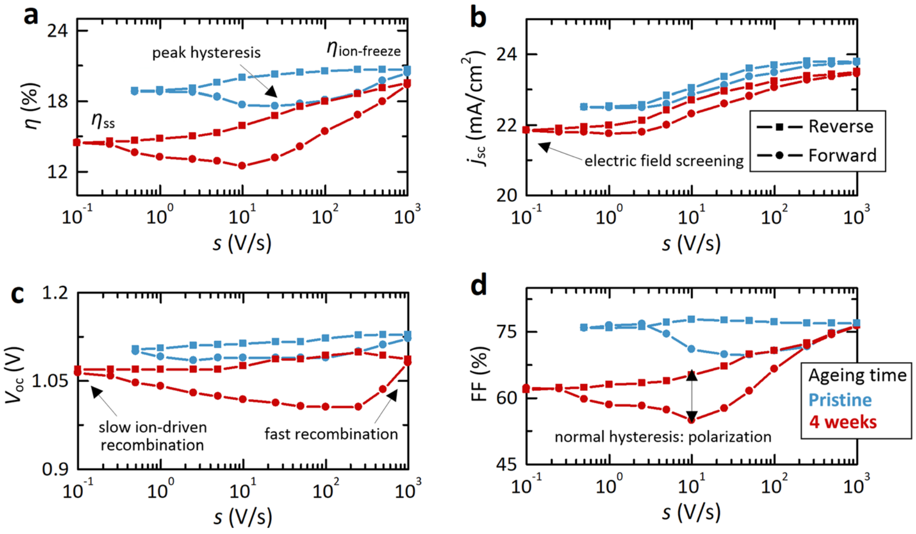

Fig. 1 Exemplified trends of the (a) efficiency η, (b) short-circuit current density j_{sc}, (c) open-circuit voltage V_{oc}, and (d) fill factor (FF) obtained from the current–voltage curves at a wide range of scan rates in reverse (squares) and forward (circles) sweep directions for fresh and degraded perovskite devices.

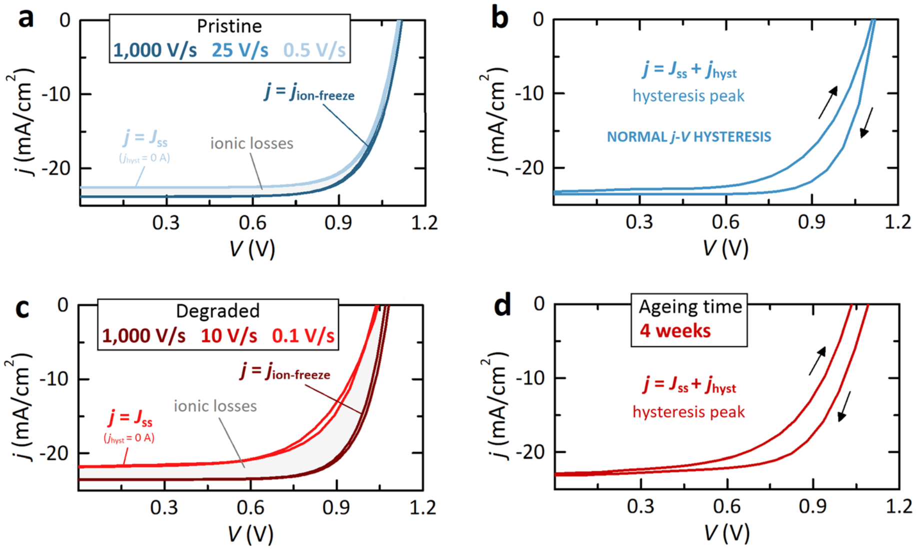

Fig. 2 Representative scan rate-dependent current–voltage curves in (a and b) pristine conditions and (c and d) after 4 weeks of ageing. 'Ion-freeze' and steady-state current–voltage curves are obtained at fast (1000 V s^{-1} in a and c) and slow sweep speeds (0.5 V s^{-1} in a and 0.1 V s^{-1} in c), respectively, at which the hysteresis disappears compared to intermediate rates (25 V s^{-1} in b and 10 V s^{-1} in d).

performance losses for our degraded perovskite devices are fundamentally due to an abrupt decrease of FF. V_{oc} and j_{sc} are affected to a lesser extent. However, this evolution exemplifies a particular case of how the performance parameters of a *nip*-type cell can change during degradation. A more comprehensive and extensive review of such changes across a wide range of device layer architectures has already been conducted in the literature.[12] Next, we will analyze the case of a specific *pin*-type device.

As a representative example, Fig. 2 shows the remarkable difference of the current–voltage curves and thus of the power conversion efficiency between fast and slow scan rates after 4 weeks of ageing. If one compares both 'ion-freeze' current–voltage curves of Fig. 2a and c, fast losses can be easily obtained by inspection.[12] Conversely, ionic losses are observed when comparing the curves at fast and slow speeds[11,12] under the same operating conditions. Fig. 2b and d show that hysteresis remains normal, not inverted, suggesting that capacitive and polarization effects[24,25] govern, for this case and commonly for high-performance and stable cells, the device operation.

Physical model of current–voltage curves in perovskite solar cells

To explain the experimental conditions that "freeze" the mobile ions during a stepwise voltage scanning, we propose a physical model that tracks the evolution of the current transient responses. The meaning of analytical variables is summarized in Table S1.

The basic solar cell device model establishes that the net extracted current in steady state or equilibrium is

$$J_{ss}(V) = J_{rec}(V) - J_{ph}(V, \Phi) \tag{1}$$

where J_{rec} and J_{ph} are, respectively, the stationary recombination current and the photocurrent in equilibrium created by charge generated per unit time and area under the incoming photon flux Φ.

For perovskite solar cells, J_{rec} must be separated into two different pathways depending on the recombination velocity. Based on the experimental impedance observations of the voltage-dependence electrical elements reported in literature,[26,27] we therefore assume the overall recombination current as[9,28]

$$J_{rec}(V) = J_{rec,fast}(V) + J_{rec,slow}(V) \tag{2}$$

with

$$J_{\text{rec, fast}}(V) = J_{f0}\, e^{\frac{qV}{n_f k_B T}} \tag{3}$$

$$J_{\text{rec, slow}}(V) = J_{d0}\, e^{\frac{qV}{n_d k_B T}} \tag{4}$$

Both components represent, respectively, the fast bulk and slow surface recombination modes with J_{f0} and J_{d0} as pre-factors, as well as n_f and n_d as ideality factors. Here q is the elementary charge, k_B the Boltzmann's constant, and T the absolute temperature.

On the other hand, we also separate the photocurrent, created by charge extraction at selective contacts and commonly affected by ion-induced field screening in perovskite solar cells, into two components. The steady-state photocurrent $J_{ph}(V, \Phi)$ is,

$$J_{ph}(V, \Phi) = j_{pho}(\Phi)\left[\eta_d + \eta_f\left(1 - \frac{V}{V_0}\right)\right] \tag{5}$$

where $j_{pho}(\Phi)$ is a pre-factor, η_d is the efficiency of charge collection by diffusion (independent of the electric field), η_f is the efficiency of charge collection by drift transport, $0 \le (\eta_d + \eta_f) \le 1$, and V_0 is a constant related to the built-in voltage. Logically, $J_{ph} = j_{pho}(\Phi)[\eta_d + \eta_f]$ at short-circuit conditions. However, the photocurrent is severely reduced during degradation,[29,30] generating a large disparity of current values close to 0 V due to charge collection issues.

In perovskite solar cells in which slow ion-assisted relaxation effects are present, an additional transient current j_{trans} is expected to be observed in experimental measurements. Thus, this fundamental analysis allows us to write a general formula for the total current[31] flowing through the perovskite solar cells j divided in terms accounting for electronic steady-state contributions and ion-assisted transient effects:

$$j = J_{\text{ss}} + j_{\text{trans}} \tag{6}$$

Note that we use uppercase letters for steady-state or instantaneous currents (J_{ss} and its terms) and lowercase letters for time-dependent currents (j_{trans} and its components) throughout the manuscript.

Ionic motion becomes evident at intermediate sweep rates, manifesting itself from hysteresis mechanisms in the current–voltage curves and underlying a multitude of phenomena, such as polarization,[24,32] delayed recombination,[32–34] or field screening.[12,29,35,36] Consequently, the relaxation current can be expressed as:

$$j_{\text{trans}} = C_{\text{g}}\frac{\mathrm{d}V}{\mathrm{d}t} + j_{\text{hyst}} \tag{7}$$

including a displacement current that charges the geometrical capacitance of the perovskite material C_{g}, but insignificant for all purposes in this study, and the hysteresis current term

$$j_{\text{hyst}} = \underbrace{C_{\text{s}}\frac{\mathrm{d}v_{\text{s}}}{\mathrm{d}t}}_{\text{polarization}} - \underbrace{\tau_{\text{d}}\frac{\mathrm{d}j_{\text{d}}}{\mathrm{d}t}}_{\text{recombination}} + \underbrace{j_{\text{ph0}}(\Phi)\frac{\eta_{\text{f}}\tau_{\text{b}}}{V_0}\frac{\mathrm{d}v_{\text{b}}}{\mathrm{d}t}}_{\text{charge collection}} \tag{8}$$

divided in (i) a polarization current, $C_{\text{s}}(\mathrm{d}v_{\text{s}}/\mathrm{d}t)$, in the sense of a surface voltage v_{s} and a capacitance C_{s},[32,37] (ii) a current j_{d} associated to secondary recombination events,[9,38–40] and (iii) a residual charge collection current expressed in terms of v_{b} as the slow component of bulk electrical field (in terms of voltage). All the components of j_{hyst} are delayed by kinetic time constants (τ_{s}, τ_{d}, and τ_{b}, respectively) due to ionic mechanisms.[41] The respective relaxation equations of the ion-controlled processes given in eqn (8) can be found in the SI.

Therefore, the limiting behavior of the hysteretic current is:

$$j_{\text{hyst}} = \begin{cases} 0\ \text{A}, \quad s \to 0 \\ C_{\text{s0}}\dfrac{V}{\tau_{\text{s}}} - J_{\text{d0}}\,\mathrm{e}^{\frac{qV}{n_{\text{d}}k_{\text{B}}T}} + j_{\text{ph0}}(\Phi)\eta_{\text{f}}\dfrac{V}{V_0}, \quad s \to \infty \end{cases} \tag{9}$$

for steady-state and 'ion-freeze' conditions, respectively.

On the one hand, the hysteresis term is zero at sufficiently low scan rates ($s \to 0$): internal ionic dynamics are equilibrated ($v_{\text{s}} \to V$, $j_{\text{d}} \to J_{\text{rec,slow}}(V)$, and $v_{\text{b}} \to V$).[13]

Under 'ion-freeze' conditions (at a scan rate sufficiently high $s \to \infty$), on the other hand, ionic polarization current is negligible ($v_{\text{s}} \to 0$), surface recombination pathway is deactivated ($j_{\text{d}} \to 0$),[42] and the charge collection efficiency by diffusion is not reduced ($v_{\text{b}} \to 0$), generating, as discussed below, the difference between η_{ss} and $\eta_{\text{ion-freeze}}$. Note that eqn (9) for high scan rates can be obtained, therefore, including a zero value for the slow ion-controlled variables in eqn (S1)–(S7). Specifically, it is important to clarify that surface recombination cannot dynamically respond during fast-hysteresis measurements (*e.g.*, under 'ion-freeze' conditions) when the applied voltage changes rapidly. The respective ion-driven current is consequently "frozen in time", unchanged during the voltage scan, and therefore does not contribute to the observed current evolution. As a result, device efficiency remains invariant upon ageing. So, we demonstrate that the 'ion-freeze' efficiency is independent of surface recombination, as evidenced by both theory and experimental measurements *via* transient analysis and Impedance Spectroscopy. This insight resolves previously reported ambiguities arising from drift-diffusion approaches[12] and contributes to a deeper understanding of the 'ion-freeze' state in perovskite solar cells.

From eqn (1)–(7), and (9), the 'ion-freeze' current may be therefore expressed as

$$j_{\text{ion-freeze}} = J_{\text{f0}}\,\mathrm{e}^{\frac{qV}{n_{\text{f}}k_{\text{B}}T}} + C_{\text{s0}}\frac{V}{\tau_{\text{s}}} - j_{\text{ph0}}(\Phi)\left[\eta_{\text{d}} + \eta_{\text{f}}\right] \tag{10}$$

In effect, the contributions of the ionic conductivity, the slow step of recombination and the bulk electric field, in terms of voltage, are negligible to the measured current j (Fig. 1a), thus obtaining that $j \sim j_{\text{ion-freeze}}$.

Transient analysis: 'ion-freeze' conditions and hysteresis window

A detailed examination of the experimental current–voltage curves in perovskite devices suggest that the shapes of the general responses are governed by the continuous voltage-dependent transient dynamics between the successive current recordings. Fig. 3 illustrates a representative example of the intricate dynamics by which the current evolves between V_{oc} and V_{oc} + 5 mV, from the step change to long time scales.

The resulting behavior is characterized by complex multiscale dynamics from the initial spike just after the voltage step, due to series resistance effects R_{s}, to the final steady-state regime, when the ions are in equilibrium. During this transition, the current response converges to an intermediate state, giving rise to the 'ion-freeze' phenomena in the current–voltage curves. Notably, the transient responses only show decays between 0 V and V_{oc} in our perovskite devices, driven primarily by polarization effects.[24,43] However, it is also plausible for the dynamics to exhibit a decay followed by a rise—or the reverse—accompanied by subsequent negative spikes,[44] if specific time constants are involved and delayed recombination or field screening become dominant factors.[41]

Fig. 3 provides a general outlook of the current waveforms and the respective labels during the classical stepwise voltage scanning used to assess device efficiencies.[45–47] Note that, however, the values of mainly the conductances and to a lesser extent the time constants can vary along the swept voltage due to the intrinsic nonlinear behavior of the solar cell and thus, further analysis is indeed necessary[48] as we will show below.

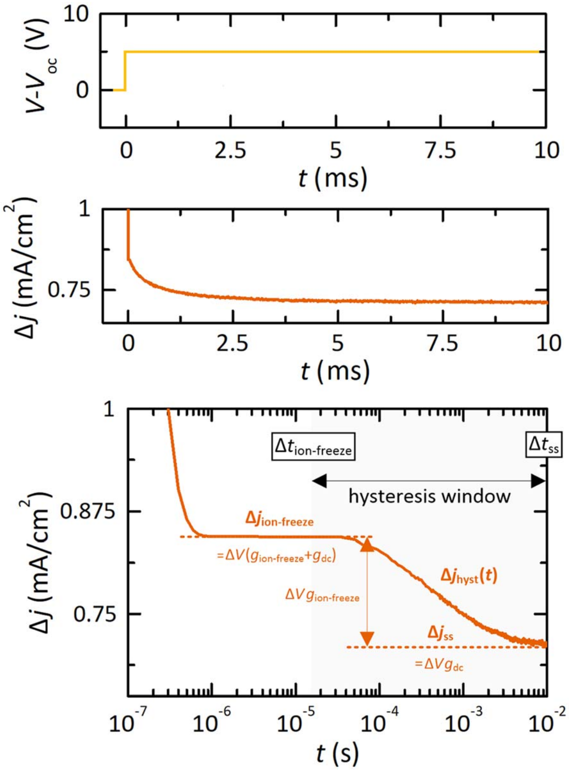

Fig. 3 Experimental example of a small amplitude time-dependent photocurrent response $\Delta j(t)$ during a stepwise voltage scanning. On the one hand, it is shown the voltage excitation ΔV, consisting of a step-size of 5 mV from V_{oc} and, on the other hand, a representative ulterior current response in linear and logarithmic scales. The specific current values are highlighted at the relevant time scales.

To analyze the dynamical properties of the perovskite solar cells during classical voltage scanning from an adequate theoretical perspective, one should consider small step-type perturbations that depart from stationary points as excitations.[45] For the measurement of cyclic voltammetry, the critical parameter is the scan rate

$$s = \frac{\Delta V}{\Delta t} \tag{11}$$

and more specifically the time duration Δt of each step during the voltage sweep since ΔV is certainly limited to maintain the linearity criteria (typically between 5 and 20 mV). s can be neither zero nor infinite as indicated by the eqn (9), but a finite value sufficiently small or large dictated by Δt. By a close inspection of Fig. 3, it is clear that the selection of the parameter Δt plays a key role in the state of the current: equilibrated, hysteretic or in the 'ion-freeze' state.

From the linearization of eqn (1) and (6)–(8), network analysis and synthesis show that the relaxation processes involved in the current shifts Δj during a voltage sweep are described according to the following relationships:[13,42]

$$\Delta j_{\mathrm{ss}} = \Delta V(g_{\mathrm{rec,fast}} + g_{\mathrm{rec,slow}} + g_{\mathrm{elect\ field}}) = \Delta V g_{\mathrm{dc}} \tag{12}$$

$$\Delta j(t) = \Delta j_{\mathrm{ss}} + \Delta j_{\mathrm{trans}}(t) \tag{13}$$

$$\Delta j_{\mathrm{trans}}(t) = \frac{\Delta V}{R_{\mathrm{s}}}\,\mathrm{e}^{-\frac{t}{\tau_{\nu}}} + \Delta j_{\mathrm{hyst}}(t) \tag{14}$$

$$\Delta j_{\mathrm{hyst}}(t) = \Delta V g_{\mathrm{ion\text{-}freeze}}\,\mathrm{e}^{-\frac{t}{\tau_{\mathrm{kin}}}} \tag{15}$$

with Δj_{ss}, $\Delta j_{\mathrm{trans}}(t)$, and $\Delta j_{\mathrm{hyst}}(t)$ as the small signal current time domain variables. The state variables of our physical model establish several internal voltage-dependent conductances[9] in the perovskite devices that determine the transient responses (*e.g.*, $g_{\mathrm{rec,fast}}$, $g_{\mathrm{rec,slow}}$, $g_{\mathrm{elect\ field}}$ or $g_{\mathrm{ion\text{-}freeze}}$ in eqn (12) and (15)). The mathematical expression of such electrical terms can be found in SI.

The graphical representation of the experimental current shift $\Delta j(t)$ of Fig. 3 has been labeled to reveal details in correspondence to eqn (12)–(15). Here, the transient current makes a transition from the initial conductivity peak (with a value of $1/R_{\mathrm{s}}$ and after describing the dielectric capacitor charging governed by $\tau_{\nu} = R_{\mathrm{s}}C_{\mathrm{g}}$) to an 'ion-freeze' conductivity state, $g_{\mathrm{ion\text{-}freeze}} + g_{\mathrm{dc}}$, that finally causes the current to decay by the ion-controlled effects towards a stationary conductance g_{dc}.

An expanded view of time-dependent photocurrents in response to stepwise voltage sweep in forward direction around V_{oc} of Fig. 4a is shown in Fig. 4b–d, as a representative example, for the perovskite devices after 4 weeks of ageing.

In the current–time profiles of Fig. 4b, all photocurrents reach steady-state conditions at the end of each step and thus, no hysteresis effects should emerge in the subsequent current–voltage curves (refer to Fig. 2c for a scan rate of 0.1 V s^{-1}). Here, we strategically select a minimum time delay Δt_{ss} to reach steady-state conditions:

$$\Delta t_{\mathrm{ss}} = \left(5 - \ln\left|\frac{g_{\mathrm{dc}}}{g_{\mathrm{ion\text{-}freeze}}}\right|\right)\tau_{\mathrm{kin}} \tag{16}$$

obtained from the constraint of $\Delta j_{\mathrm{ss}} \gg \Delta j_{\mathrm{hyst}}(\Delta t_{\mathrm{ss}})$ with a 1% criterion.[13,49]

Subsequently the optimal scan rate s_{ss} to accelerate the elimination of the hysteresis is

$$s_{\mathrm{ss}} = \frac{\Delta V}{\Delta t_{\mathrm{ss}}} = \frac{\Delta V}{\tau_{\mathrm{kin}}}\left[5 - \ln\left|\frac{g_{\mathrm{dc}}}{g_{\mathrm{ion\text{-}freeze}}}\right|\right]^{-1} \tag{17}$$

Note that, to simplify the problem, we assumed that the slow physical processes exhibit approximately the same kinetic time constant τ_{kin} independently on the voltage, which is a realistic assumption according to experimental observations.[13,28,40]

With lower experimental delay times, slow and non-steady-state operation of the *nip*-type perovskite solar cells gradually influence the electrical responses shown in Fig. 4c. As a result, one obtains increasing residual currents as a natural consequence of the past activity. Physically speaking, the anomalous ion migration cannot respond as fast to each voltage stimuli introduced during cyclic voltammetry and therefore the current is interrupted before the value of the hysteretic current is negligible, $\Delta j_{\mathrm{hyst}}(t) \neq 0$ A. In this way, the shape of the current–voltage curve is altered due to the hysteresis phenomenon (refer to Fig. 2d), driven by the presence of mobile ions.

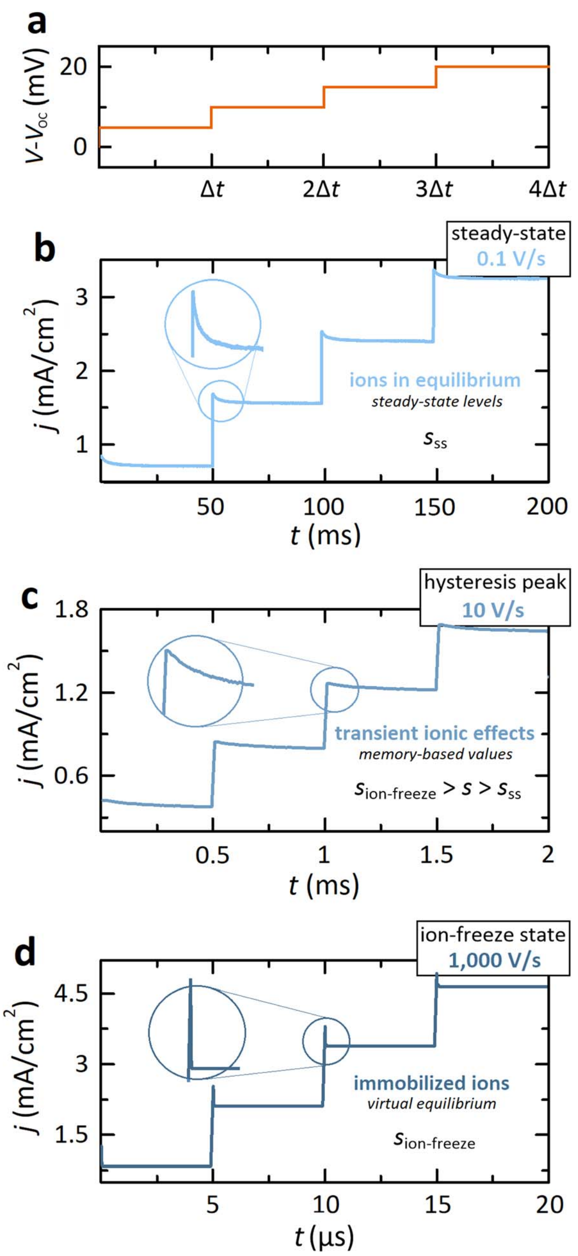

Fig. 4 Illustrative photocurrent profile as a function of time at a (a) forward stepwise voltage scan between V_{oc} and V_{oc} + 20 mV depending on the duration of the 5 mV voltage steps: (b) 50 ms (scan rate of 0.1 V s^{-1}), (c) 0.5 ms (scan rate of 10 V s^{-1}), and (d) 5 µs (scan rate of 1000 V s^{-1}) corresponding, respectively, to the equilibrium situation, 'peak hysteresis', and 'ion-freeze' state of the current–voltage curves shown in Fig. 2c and d for our perovskite devices.

Finally, Fig. 4d shows that the pseudo-instantaneous currents uniquely emerge at sufficiently low values of Δt. Current responses are indeed pseudo-stabilized in an intermediate state in which the hysteretic response of eqn (15) is constant, $\Delta j_{\text{hyst}} = \Delta V g_{\text{ion-freeze}}$, and thus the ions are immobilized without generating notorious discrepancies between the current–voltage relationship in forward and reverse scans (refer to Fig. 2c for a scan rate of 1000 mV s^{-1}). Only the charging of the bulk capacitor and the fast step of recombination processes take place at each voltage step during the voltage cycling. The key here is that the contribution of the 'ion-freeze' conductivity $g_{\text{ion-freeze}}$ is not reduced by the respective exponential term of eqn (15).

Mathematically speaking, this condition requires that $e^{-t/\tau_{\text{kin}}} \sim 1$, which implies that only the first term of the MacLaurin series expansion of the exponential function is operative, $1 \gg (t/\tau_{\text{kin}})$. Therefore, the time $\Delta t_{\text{ion-freeze}}$ required to neutralize the movement of ions and approach an 'ion-freeze' state, in practice, is that for which

$$\Delta t_{\text{ion-freeze}} \ll \tau_{\text{kin}} \tag{18}$$

giving rise, at such time scales, to the 'ion-freeze' current:

$$\Delta j_{\text{ion-freeze}} = \Delta V(g_{\text{dc}} + g_{\text{ion-freeze}}) \tag{19}$$

by considering that the constraint of eqn (18) is satisfied by selecting a value for Δt that is 100 times smaller than τ_{kin}. A value of scan rate to suppress the ion mobility, $s_{\text{ion-freeze}}$, can be obtained as

$$s_{\text{ion-freeze}} = \frac{\Delta V}{\Delta t_{\text{ion-freeze}}} = 100\frac{\Delta V}{\tau_{\text{kin}}} \tag{20}$$

being thus the optimal fast scan speed to obtain the 'ion-freeze' efficiency of perovskite solar cells. Note that we consider again the 1% criterion as in eqn (16) and (17).

Hence, the solar cell characterizers can obtain a current–voltage curve devoid of hysteresis effects at the voltage scan speeds given by eqn (17) and (20), corresponding to the equilibrium and 'ion-freeze' states, respectively. For intermediate values ($\Delta t_{\text{ion-freeze}} < \Delta t < \Delta t_{\text{ss}}$), hysteresis phenomena become apparent in the current–voltage curves. Thus, this work, for the first time in literature, defines a "hysteresis window"

$$\frac{\Delta V}{\tau_{\text{kin}}}\left[5 - \ln\left|\frac{g_{\text{dc}}}{g_{\text{ion-freeze}}}\right|\right]^{-1} < s < 100\frac{\Delta V}{\tau_{\text{kin}}} \tag{21}$$

that effectively enables a specific range of scan rates to observe hysteresis in the current–voltage characteristics of perovskite solar cells.

Note that, experimentally, τ_{kin} does not maintain a strict constant value, particularly for aged devices throughout the swept voltage range, as can be seen in the plot of the relaxation times of Fig. 5a obtained from time- and frequency-resolved techniques. This fact requires that experimentalists select an appropriate value based on the previously outlined rules: the maximum (minimum) value of τ_{kin} for eqn (16) and (17) (eqn (18) and (20)).

Perspective of equivalent circuits: impedance measurements

Impedance analysis was also carried out for verification and illustrative purposes of the theory and the exemplificative decay time transient of Fig. 3.

First, we present the theoretical admittance response of our model for a small sinusoidal perturbation of angular frequency ω:

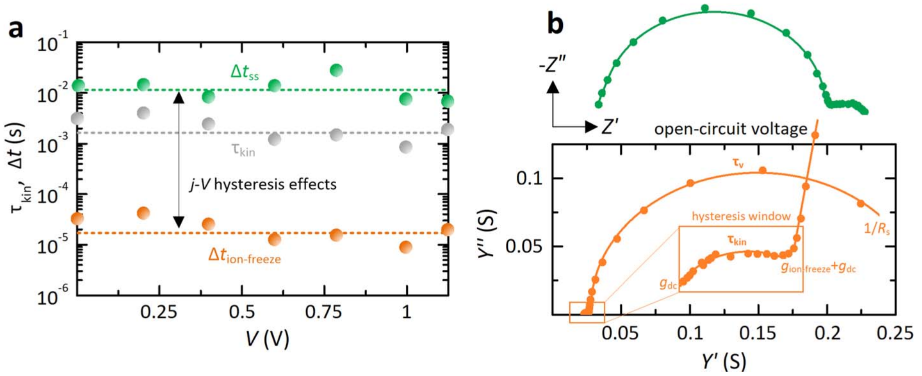

Fig. 5 (a) Time constants extracted from the voltage-dependent transient and impedance responses. (b) Complex plane admittance spectrum measured at V_{oc} in a degraded device. Key conductance values are indicated in the experimental spectra to obtain a time-scale mapping of the current–voltage characteristics for perovskite solar cells: dc conditions, hysteresis window, and 'ion-freeze' state.

$$Y(j\omega) = g_{\mathrm{dc}} + \frac{1}{R_{\mathrm{s}}}\frac{j\omega}{j\omega + \dfrac{1}{\tau_{\mathrm{v}}}} + \frac{j\omega g_{\text{ion-freeze}}}{j\omega + \dfrac{1}{\tau_{\mathrm{kin}}}} \tag{22}$$

where, on the one hand, pure electronic processes are controlled by τ_v and, on the other hand, slow ion-induced mechanisms are governed by the τ_{kin}. For the previous results, it is clear that $g_{\text{ion-freeze}} > 0$.[13] Note that the 'ion-freeze' conductance could be lower than zero if negative capacitance features, in form of transient spikes[44] or inductive loops,[37,40,50–52] are present in the time- and frequency-resolved experiments, respectively.

We observe that the perovskite devices respond with a double capacitive arc in the complex plane impedance and admittance plots[26,53] of Fig. 5b, which is strictly equivalent to the doubling decay of the current responses shown in Fig. 3 and 4. Apart from the initial high frequency, there are two additional frequential values $f_{\text{ion-freeze}}$ and f_{dc} (experimentally, around 200 kHz and 20 Hz) in which the admittance exhibits a single conductance value with zero susceptance; *i.e.*, $Y'(j\omega)$ is strictly equal to $g_{\text{ion-freeze}} + g_{dc}$ or g_{dc} and $Y''(j\omega) = 0$. Note that $\omega = 2\pi f$. There is, in fact, a close relationship between these frequencies and the values of time $\Delta t_{\text{ion-freeze}}$ and Δt_{ss} leading to free-hysteresis current–voltage curves, as some of the authors indicated in a previous work.[42]

The hysteresis window is also highlighted in Fig. 5a, which is located in the low-frequency range of $f_{\text{ion-freeze}} > f > f_{dc}$. To select such specific values, it is important to note that the concept of admittance, not impedance, must be analyzed, as only the former is controlled in voltage,[41] like the current–voltage curves. For a more detailed impedance-based analysis, additional measurements at different operating bias voltage points would be necessary, which have already been presented in detail by the authors in other works.[49,54]

From *nip*- to *pin*-type cells in the experimental visualization of 'ion-freeze' regime

Finally, it is important to point out that we also investigated *pin*-type devices (Fig. S1), where we observed a similar evolution in the scan rate-dependent efficiency, current–voltage characteristics, transient current responses, and immittance spectra.

However, certain differences in the characteristic time scales are observed: the 'ion-freeze' state, the 'peak hysteresis', and the equilibrium regime occur at faster scan rates compared to our *nip*-type cells, which is consistent with previous reports.[17,25,49] Additionally, the 'ion-freeze' regime for this device is narrower (see, specifically, Fig. S1c), an observation of particular interest. This peculiar behavior correlates with the smaller separation between τ_v and τ_{kin} in the *pin*-type architecture relative to the *nip*-type device. In short, we present experimental evidence that confirms the validity of the conclusions presented here in the SI.

Conclusions

This work reveals key physical characteristics of ion dynamics in perovskite solar cells, shedding light on the complex interplay between ionic motion and photovoltaic performance. By identifying characteristic time scales associated with ion immobilization, we establish the conditions under which ionic contributions to current–voltage behavior can be suppressed, enabling a direct quantification of ion-induced efficiency losses. Our findings encompass critical physical phenomena (including polarization effects, multi-timescale recombination dynamics, and electric field screening) that govern the energetic landscape of perovskites under operation. Notably, we identify for the first time a defined "hysteresis window", a specific scan-rate range in which mobile ion motion gives rise to observable current–voltage hysteresis, thereby linking ion kinetics to measurable device behavior. These insights are supported through complementary experimental techniques such as cyclic voltammetry, chronoamperometry, and impedance spectroscopy, applied to high-performance perovskite devices. Together, these results offer a refined physical understanding of time-dependent ionic processes, providing a foundation for improved efficiency characterization and stability strategies in perovskite photovoltaics.

Conflicts of interest

There are no conflicts to declare.

Data availability

The data that support the findings of this study are available from the corresponding authors, upon reasonable request.

Supplementary information: theory of ion-controlled processes of perovskite solar cells; conductances of the complete device model; summary of analytical variables; application in *pin*-type cells. See DOI: **https://doi.org/10.1039/d5el00137d**.

Acknowledgements

This work has received funding from the Universidad Rey Juan Carlos, project numbers M3704 and M3712. J. Bisquert thank Grant EUR2022-134045 funded by MICIU/AEI/10.13039/501100011033 and European Union NextGenerationEU/PRTR. Michael Saliba and Chittaranjan Das thank the German Research Foundation (DFG) for funding (SPP 2196, 431314977/GRK 2642). Michael Saliba also acknowledges funding from the European Research Council under the Horizon Europe Program (LOCAL-HEAT, Grant Agreement 101041809) and the German Bundesministerium für Bildung and Forschung (BMBF), project "NETPEC" (01LS2103E).

References

1 N.-G. Park, M. Grätzel, T. Miyasaka, K. Zhu and K. Emery, *Nat. Energy*, 2016, **1**, 16152.
2 Y. Rong, Y. Hu, A. Mei, H. Tan, M. I. Saidaminov, S. I. Seok, *et al.*, *Science*, 2018, **361**(6408), eaat8235.
3 W. Meng, K. Zhang, A. Osvet, J. Zhang, W. Gruber, *et al.*, *Joule*, 2022, **6**(2), 458–475.
4 L. Meng, J. You, Y. Yang, L. Meng, J. You, *et al.*, *Nat. Commun.*, 2018, **9**, 5265.
5 J. Thiesbrummel, V. M. Le Corre, F. Peña-Camargo, L. Perdigón-Toro, F. Lang, *et al.*, *Adv. Energy Mater.*, 2021, **11**(34), 202101447.
6 J. A. Kress, C. Quarti, Q. An, S. Bitton, N. Tessler, *et al.*, *ACS Energy Lett.*, 2022, **7**(10), 3302–3310.
7 L. J. F. Hart, F. J. Angus, Y. Li, A. Khaleed, P. Calado, *et al.*, *Energy Environ. Sci.*, 2024, **17**(19), 7107–7118.
8 E. L. Unger, E. T. Hoke, C. D. Bailie, W. H. Nguyen, A. R. Bowring, *et al.*, *Energy Environ. Sci.*, 2014, **7**, 3690–3698.
9 E. H. Balaguera and J. Bisquert, *Small*, 2025, **21**(2), 2409534.
10 W. Tress, N. Marinova, T. Moehl, S. M. Zakeeruddin, M. K. Nazeeruddin, *et al.*, *Energy Environ. Sci.*, 2015, **8**, 995–1004.
11 V. M. Le Corre, J. Diekmann, F. Peña-Camargo, J. Thiesbrummel, N. Tokmoldin, *et al.*, *Sol. RRL*, 2022, **6**(4), 2100772.
12 J. Thiesbrummel, S. Shah, E. Gutierrez-Partida, F. Zu, F. Peña-Camargo, *et al.*, *Nat. Energy*, 2024, **9**, 1–13.
13 E. H. Balaguera and J. Bisquert, *ACS Energy Lett.*, 2024, **9**(2), 478–486.
14 J. Diekmann, F. Peña-Camargo, N. Tokmoldin, J. Thiesbrummel, J. Warby, *et al.*, *J. Phys. Chem. Lett.*, 2023, **14**(18), 4200–4210.
15 H. J. Snaith, A. Abate, J. M. Ball, G. E. Eperon, T. Leijtens, *et al.*, *J. Phys. Chem. Lett.*, 2014, **5**(9), 1511–1515.
16 S. van Reenen, M. Kemerink and H. J. Snaith, *J. Phys. Chem. Lett.*, 2015, **6**(19), 3808–3814.
17 P. Calado, A. M. Telford, D. Bryant, X. Li, J. Nelson, *et al.*, *Nat. Commun.*, 2016, **7**(1), 13831.
18 M. T. Neukom, S. Züfle, E. Knapp, M. Makha, R. Hany, *et al.*, *Sol. Energy Mater. Sol. Cells*, 2017, **169**, 159–166.
19 M. V. Khenkin, E. A. Katz, A. Abate, G. Bardizza, J. J. Berry, *et al.*, *Nat. Energy*, 2020, **5**(1), 35–49.
20 A. Pockett and M. J. Carnie, *ACS Energy Lett.*, 2017, **2**(7), 1683–1689.
21 D. A. Jacobs, Y. Wu, H. Shen, C. Barugkin, F. J. Beck, *et al.*, *Phys. Chem. Chem. Phys.*, 2017, **19**(4), 3094–3103.
22 C. Eames, J. M. Frost, P. R. F. Barnes, B. C. O'Regan, A. Walsh, *et al.*, *Nat. Commun.*, 2015, **6**(1), 7497.
23 D.-H. Kang and N.-G. Park, *Adv. Mater.*, 2019, **31**(34), 201805214.
24 B. Chen, M. Yang, X. Zheng, C. Wu, W. Li, *et al.*, *J. Phys. Chem. Lett.*, 2015, **6**(23), 4693–4700.
25 E. Hernández-Balaguera, B. Romero, B. Arredondo, G. del Pozo, M. Najafi, *et al.*, *Nano Energy*, 2020, **78**, 105398.
26 I. Zarazua, G. Han, P. P. Boix, S. Mhaisalkar, F. Fabregat-Santiago, *et al.*, *J. Phys. Chem. Lett.*, 2016, **7**(24), 5105–5113.
27 O. Almora, K. T. Cho, S. Aghazada, I. Zimmermann, G. J. Matt, *et al.*, *Nano Energy*, 2018, **48**, 63–72.
28 C. Gonzales, A. Guerrero and J. Bisquert, *J. Phys. Chem. C*, 2022, **126**(32), 13560–13578.
29 A. Schiller, S. Jenatsch, B. Blülle, M. A. T. Cachafeiro, F. Ebadi, *et al.*, *J. Phys. Chem. Lett.*, 2024, **15**(45), 11252–11258.
30 W. Clarke, P. J. Cameron and G. Richardson, *J. Phys. Chem. Lett.*, 2024, **15**(47), 11730–11736.
31 J. Bisquert, *Adv. Energy Mater.*, 2024, **14**(26), 202400442.
32 S. Ravishankar, O. Almora, C. Echeverría-Arrondo, E. Ghahremanirad, C. Aranda, *et al.*, *J. Phys. Chem. Lett.*, 2017, **8**(5), 915–921.
33 A. O. Alvarez, R. Arcas, C. A. Aranda, L. Bethencourt, E. Mas-Marzá, *et al.*, *J. Phys. Chem. Lett.*, 2020, **11**(19), 8417–8423.
34 W. Tress, J. P. C. Baena, M. Saliba, A. Abate and M. Graetzel, *Adv. Energy Mater.*, 2016, **6**(19), 1600396.
35 M. Diethelm, T. Lukas, T. J. Smith, A. Dasgupta, P. Caprioglio, *et al.*, *Energy Environ. Sci.*, 2025, **18**(3), 1385–1397.
36 R. A. Belisle, W. H. Nguyen, A. R. Bowring, P. Calado, P. Calado, X. Li, *et al.*, *Energy Environ. Sci.*, 2017, **10**(1), 192–204.
37 E. Ghahremanirad, A. Bou, S. Olyaee and J. Bisquert, *J. Phys. Chem. Lett.*, 2017, **8**(7), 1402–1406.
38 J.-P. Correa-Baena, S.-H. Turren-Cruz, W. Tress, A. Hagfeldt, C. Aranda, *et al.*, *ACS Energy Lett.*, 2017, **2**(3), 681–688.
39 A. Guerrero, G. Garcia-Belmonte, I. Mora-Sero, J. Bisquert, Y. S. Kang, *et al.*, *J. Phys. Chem. C*, 2016, **120**(15), 8023–8032.
40 F. Ebadi, N. Taghavinia, R. Mohammadpour, A. Hagfeldt and W. Tress, *Nat. Commun.*, 2019, **10**, 1574.
41 E. Hernández-Balaguera and J. Bisquert, *Adv. Funct. Mater.*, 2024, **34**(6), 2308678.

42 E. H. Balaguera and J. Bisquert, *Energy Fuels*, 2025, **39**(7), 3638–3648.
43 E. Hernández-Balaguera, G. del Pozo, B. Arredondo, B. Romero, C. Pereyra, *et al.*, *Sol. RRL*, 2021, **5**(4), 2000707.
44 E. Hernández-Balaguera and J. Bisquert, *ACS Energy Lett.*, 2022, **7**(8), 2602–2610.
45 H.-S. Kim and N.-G. Park, *J. Phys. Chem. Lett.*, 2014, **5**(17), 2927–2934.
46 E. Hernández-Balaguera, B. Arredondo, G. del Pozo and B. Romero, *Commun. Nonlinear Sci. Numer. Simul.*, 2020, **90**, 105371.
47 J. Bisquert, *PRX Energy*, 2024, **3**, 011001.
48 A. Guerrero, J. Bisquert and G. Garcia-Belmonte, *Chem. Rev.*, 2021, **121**, 14430–14484.
49 E. Hernández-Balaguera, L. Muñoz-Díaz, C. Pereyra, M. Lira-Cantú, M. Najafi, *et al.*, *Mater. Today Energy*, 2022, **27**, 101031.
50 J. Bisquert and A. Guerrero, *J. Am. Chem. Soc.*, 2022, **144**(13), 5996–6009.
51 E. Hernández-Balaguera, B. Arredondo, C. Pereyra and M. Lira-Cantú, *J. Power Sources*, 2023, **560**, 232614.
52 C. A. Aranda, A. O. Alvarez, V. S. Chivrony, C. Das, M. Rai, *et al.*, *Joule*, 2024, **8**(1), 241–254.
53 E. Hernández-Balaguera, B. Romero, M. Najafi and Y. Galagan, *Adv. Mater. Interfaces*, 2022, **9**(9), 2102275.
54 J. Bisquert, A. Guerrero and C. Gonzales, *ACS Phys. Chem. Au*, 2021, **1**(1), 25–44.